International Journal of Emerging Technologies and Advanced Applications

Accurate Analysis of the Electrical Performance of Hypersonic Vehicle Radomes under Thermo-mechanical Effects

Pengfei Zhao[1], Xinyuan Zhou[1], Xuefeng Cheng[2], Yi Ren[2*], Shengpeng Zhang[1]
[1] Aerospace Science & Industry Corporation, Defense Technology Research and Test Center, Beijing 100854, China
[2]Electronic Engineering, Xidian University, Xi'an 710071, China
renyi_cq@hotmail.com

***Abstract*—Under extreme flight conditions, radomes applied to hypersonic vehicles must simultaneously endure intense aerodynamic heating and complex mechanical loads, leading to changes in material properties and structural configuration that significantly affect antenna electrical performance. This investigation presents an in-depth analysis of radome electrical performance under thermo-mechanical effects and proposes a precise integrated electrical performance analysis methodology for radome-antenna systems based on the finite element method. The approach establishes a coupled radome-antenna model through finite element analysis while considering material property variations induced by thermo-mechanical coupling. Based on temperature distribution characteristics obtained from finite element analysis, the radome undergoes layered processing where electrical parameter distributions are established layer by layer according to temperature-dependent material characteristics, providing a more realistic representation of radome electrical performance variations under high-temperature conditions. The proposed modeling methodology is validated through antenna radiation analysis under typical operating frequency bands, demonstrating excellent agreement with experimental observations and providing crucial insights for next-generation aerospace system design optimization.**

***Index Terms*—Hypersonic vehicle, Radome, Thermo-mechanical effects, Finite element method, Electrical performance modeling**

I. Introduction

With the rapid advancement of aerospace technology, hypersonic vehicles have emerged as a critical research focus in the aerospace domain due to their advantages in high-speed operation, long-range capability, and rapid response characteristics. These capabilities address the urgent requirements for efficient global response systems in contemporary aviation applications. However, hypersonic vehicles encounter extreme aerodynamic environments during flight operations, with radomes at the vehicle nose experiencing intense aerodynamic heating and complex mechanical loading conditions.

These thermo-mechanical effects not only cause material property degradation but also induce structural configuration changes, significantly affecting antenna electrical performance [1]–[3]. Consequently, accurate analysis of radome electrical performance under thermo-mechanical coupling effects has become essential research content in the aerospace field to ensure proper antenna and radome operation during high-speed flight conditions.

Radomes serve as critical components for hypersonic vehicles, with primary functions including antenna protection from external environmental influences while maintaining electromagnetic wave transmission capabilities. During high-speed flight operations, non-uniform temperature distribution characteristics across the radome surface cause dynamic electromagnetic property variations. For instance, during high Mach number flight, radome surface temperatures may exceed $1500\,^{\circ}\mathrm{C}$, creating high-temperature environments that significantly alter radome material properties such as dielectric constant and loss tangent, subsequently affecting antenna radiation patterns, gain, and bandwidth characteristics.

Traditional radome electrical performance modeling methodologies primarily focus on single electromagnetic simulations, often neglecting thermo-mechanical effect influences. However, as flight velocities continue increasing, thermo-mechanical effects become increasingly significant. Recent research efforts have attempted to incorporate thermo-mechanical effects into radome electrical performance modeling [4], [5]. For example, thermo-mechanical coupling analysis of radomes through finite element methods combined with electromagnetic simulation software for electrical performance prediction has been investigated. Nevertheless, such approaches typically exhibit certain limitations, including excessive model simplification and unreasonable material parameter assumptions.

Furthermore, hypersonic vehicle radome structures are typically complex, requiring design considerations of multiple factors including material thermal stability, mechanical strength, and electromagnetic compatibility. In practical applications,

Copyright: © 2025 The Author(s); CC BY-NC 4.0.
Exclusive licensee IJETAA.

ISSN:3006-2985(Print)
ISSN:3006-9297(Online)

radome material parameters vary dynamically with temperature and stress changes. Therefore, establishing an electrical performance model capable of accurately reflecting these variations becomes critically important.

To overcome existing methodology limitations, this investigation proposes a finite element-based integrated electrical performance analysis approach for radome-antenna systems. This methodology accurately simulates radome mechanical and thermal responses under thermo-mechanical coupling through finite element analysis and performs radome layering based on temperature distribution, assigning different electromagnetic material parameters to each layer. This layering approach provides more realistic representation of radome electrical performance variations under high-temperature environments. The methodology effectiveness and accuracy are demonstrated through validation with two antenna examples operating in typical frequency bands.

II. Electromagnetic Field Vector Finite Element Modeling Theory

Finite element methods are classified into frequency-domain and time-domain approaches [7]. For general time-harmonic electromagnetic fields, the frequency-domain vector wave equation for the electric field is expressed as:

$$\nabla \times \mu_r^{-1} \nabla \times \vec{E} - k_0^2 \varepsilon_r \vec{E} = -j\omega\mu_0 \vec{J} \tag{1}$$

where $\vec{E}$ represents electric field intensity, $\vec{B}$ denotes magnetic flux density, $\vec{H}$ is magnetic field intensity, $\vec{D}$ represents electric displacement vector, and $\vec{J}$ denotes externally applied current source excitation. ε_r and μ_r represent relative permittivity and relative permeability, respectively, k_0=$\omega\sqrt{\mu_0\varepsilon_0}$ denotes the free space wave number, and Z_0 represents free space wave impedance.

Applying vector basis functions $\vec{W}$ as test functions and taking the inner product with Equation (1) yields:

$$\begin{aligned} &\int_{\Omega_e} \mu^{-1}(\nabla \times \vec{W}) \cdot (\nabla \times \vec{E}) - k_0^2 \varepsilon_r \vec{W} \cdot \vec{E}\, dv \\ &+ \int_{\partial\Omega} \nabla \times \vec{W} \cdot (\mu^{-1} \nabla \times \vec{E})\, ds = -jk_0 Z_0 \int_{\Omega} \vec{W} \cdot \vec{J}\, dv \end{aligned} \tag{2}$$

where dv denotes the volume integration element, ds represents the surface integration element, and $\partial\Omega$ denotes the boundary surface of computational domain Ω.

Vector basis functions $\vec{W}$ in finite element analysis are defined on mesh elements. Finite element mesh elements include various types such as tetrahedral and hexahedral elements. This investigation primarily employs tetrahedral elements for computational domain discretization.

As illustrated in Fig. 1, first-order vector basis functions represent the six edge vector basis functions of the tetrahedron, defined as:

$$\vec{W}_i = L_{i1}\nabla L_{i2} - L_{i2}\nabla L_{i1}, \quad i = 1, 2, \ldots, 5, 6 \tag{3}$$

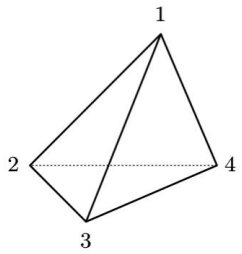

Fig. 1. Low-order tetrahedral mesh element schematic diagram

where $L_i = \frac{V_i}{V}$, $(i = 1, 2, 3, 4)$ represents the volume of four smaller tetrahedra formed by connecting point i as a vertex to the four faces of the tetrahedron. i_1 and i_2 represent the local node numbers of the i-th edge of the tetrahedron.

For second-order hierarchical vector basis functions, the total number of basis functions is 20, with two edge vector basis functions on each tetrahedral edge and two face vector basis functions on each face. The edge vector basis functions are expressed as:

$$\vec{W}_i^{e_1} = L_{i1}\nabla L_{i2} - L_{i2}\nabla L_{i1}, \quad i = 1, 2, \ldots, 5, 6 \tag{4}$$

$$\vec{W}_i^{e_2} = L_{i1}\nabla L_{i2} - L_{i2}\nabla L_{i1}, \quad i = 1, 2, \ldots, 5, 6 \tag{5}$$

where the superscript $e_1 1$ denotes the first edge vector basis function on the edge. The face vector basis functions are given by:

$$\vec{W}_i^{f_1} = L_{i3}(L_{i1}\nabla L_{i2} - L_{i2}\nabla L_{i1}), \quad i = 1, 2, 3, 4 \tag{6}$$

$$\vec{W}_i^{f_2} = L_{i2}(L_{i3}\nabla L_{i1} - L_{i1}\nabla L_{i3}), \quad i = 1, 2, 3, 4 \tag{7}$$

where subscripts i_1, i_2, and i_3 represent local node numbers on the i-th face of the tetrahedron, and superscripts f_1 and f_2 denote the first and second face basis functions on the face, respectively.

III. General Form of Basis Functions on Non-conformal Meshes

According to finite element theory, methods for improving finite element solution accuracy are classified into two categories. The first approach maintains constant mesh element sizes while increasing basis function order within mesh elements to achieve higher solution accuracy. The second method reduces mesh element sizes, increasing the number of unknowns in the system matrix to obtain higher discretization approximation accuracy.

During mesh generation, meshes can be classified as conformal or non-conformal based on the existence of hanging nodes. For non-conformal meshes, as shown in Fig. 2, adjacent elements do not require forced sharing of the same face or edge. This characteristic of non-conformal meshes significantly reduces the required mesh quantity for the overall model.

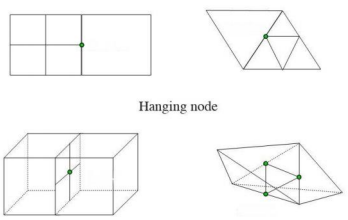

Fig. 2. Typical non-conformal mesh schematic diagram

As illustrated in Fig. 3, non-conformal interfaces consist of master and slave surfaces, where master surfaces belong to elements with lower refinement levels on both sides of the interface, while slave surfaces belong to elements with higher refinement levels. Correspondingly, edges on master surfaces are master edges, and edges on slave surfaces are slave edges.

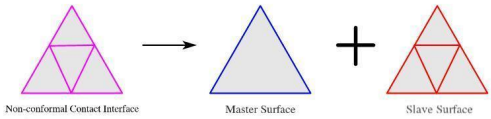

Fig. 3. Non-conformal interface detail for tetrahedral element refinement

At non-conformal interfaces, basis functions do not satisfy tangential continuity requirements. Therefore, linear interpolation methods must be employed to process basis functions at non-conformal interfaces to ensure tangential continuity. When elements use first-order hierarchical vector basis functions, master and slave surfaces contain only edge basis functions, with edge and basis function numbering shown in Fig. 4.

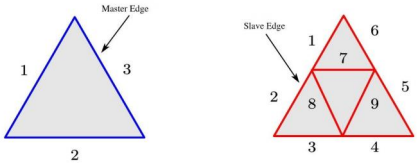

Fig. 4. Edge numbering and first-order basis function numbering for master and slave surfaces at non-conformal mesh interfaces

Edge basis functions on master surfaces can be linearly represented by edge basis functions on slave surfaces, defined by the following equation:

$$\begin{bmatrix}\vec{W}_1^e\\ \vec{W}_2^e\\ \vec{W}_3^e\end{bmatrix} = C\begin{bmatrix}\vec{w}_1^e\\ \vec{w}_2^e\\ \vdots\\ \vec{w}_8^e\\ \vec{w}_9^e\end{bmatrix} = \begin{bmatrix}c_{1,1} & c_{1,2} & \cdots & c_{1,8} & c_{1,9}\\ c_{2,1} & c_{2,2} & \cdots & c_{2,8} & c_{2,9}\\ c_{3,1} & c_{3,2} & \cdots & c_{3,8} & c_{3,9}\end{bmatrix}\begin{bmatrix}\vec{w}_1^e\\ \vec{w}_2^e\\ \vdots\\ \vec{w}_8^e\\ \vec{w}_9^e\end{bmatrix} \tag{8}$$

where $\mathbf{C}$ represents the basis function transformation coefficient matrix to be determined. Taking any point on the first edge of the slave surface and defining vector basis functions at that point with the edge unit direction vector $\vec{n}_1$, Equation (8) can be rewritten by taking inner products with $\vec{n}_1$ on both sides. According to edge vector basis function characteristics, edge vector basis functions possess tangential components only on their defining edges with constant tangential components, and no tangential components on other edges. Thus, Equation (8) becomes:

$$\begin{bmatrix}\vec{W}_1^e\cdot\vec{n}_1\\ \vec{W}_2^e\cdot\vec{n}_2\\ \vec{W}_3^e\cdot\vec{n}_3\end{bmatrix} = \begin{bmatrix}\vec{W}_1^3\cdot\vec{n}_1\\ 0\\ 0\end{bmatrix} = \begin{bmatrix}c_{1,1} & c_{1,2} & \cdots & c_{1,8} & c_{1,9}\\ c_{2,1} & c_{2,2} & \cdots & c_{2,8} & c_{2,9}\\ c_{3,1} & c_{3,2} & \cdots & c_{3,8} & c_{3,9}\end{bmatrix}\begin{bmatrix}\tilde{w}_1^e\\ \tilde{w}_2^e\\ \vdots\\ \tilde{w}_5^e\\ \tilde{w}_6^e\\ 0\\ 0\end{bmatrix} \tag{9}$$

Similar processing for remaining edges provides the specific form of $\mathbf{C}$. For higher-order basis functions, the treatment approach is similar and will not be elaborated here.

IV. Electromagnetic Modeling of Radomes Considering Thermo-mechanical Coupling Effects

Radome electromagnetic characteristics significantly influence antenna system performance, with primary variables including electromagnetic properties of radome materials, configuration schemes, geometric shapes, and dimensional specifications.

From an electromagnetic materials perspective, substrate relative permittivity and dielectric loss tangent values constitute core parameters determining radome electrical characteristics. Materials with smaller dielectric constants and lower loss factors facilitate electromagnetic energy transmission. Additionally, material moisture resistance, environmental stability, and chemical corrosion resistance affect transmission performance. Moisture-absorbing materials may experience performance degradation under high-humidity conditions, necessitating selection of composite materials with low moisture absorption rates and excellent environmental adaptability. In current engineering practice, silicon nitride ceramic materials have become ideal choices for hypersonic vehicle antenna protection structures due to their ability to withstand high-temperature environments while maintaining minimal electromagnetic parameter variations [6], [8]–[10].

From structural engineering perspectives, different design schemes significantly alter transmission characteristics. Single-layer homogeneous structures, while simple in fabrication, tend to produce strong interface reflections under large-angle incidence and different polarization modes. Sandwich configurations can reduce reflection wave intensity through phase interference effects. Composite structures with honeycomb cores similarly utilize multiple reflection destructive interference to enhance transmission efficiency.

Regarding shape design, configurations employing revolution geometries, aerodynamically compliant elliptical profiles, and low-drag streamlined shapes both reduce aerodynamic drag and optimize electromagnetic wave transmission paths.

For high-speed platforms such as aircraft and missiles, sharp conical radomes effectively reduce aerodynamic drag but require careful evaluation of electromagnetic beam shadowing effects.

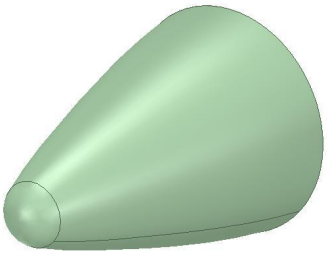

Fig. 5. Typical hypersonic vehicle radome appearance schematic diagram

Figure 5 presents a radome designed for hypersonic vehicle applications, employing a single-layer homogeneous structure with approximately $6\,\mathrm{mm}$ wall thickness and fused silica ceramic material. When high-speed airflow encounters radome external surfaces, intense aerodynamic heating effects occur, causing rapid surface temperature increases. When temperatures reach radome melting points, ablation phenomena occur, with continuous ablation gradually reducing radome thickness and affecting electromagnetic wave transmission characteristics. During ablation processes, material gasification and decomposition create surface layers with different electromagnetic parameters, influencing antenna system radiation characteristics.

After obtaining radome conditions under high Mach number motion, the post-ablation radome appearance is shown in Fig. 6, while Fig. 7 presents overall radome wall temperature distribution. Results indicate radome nose temperatures of approximately $1470\,^{\circ}\mathrm{C}$ with gradient temperature variations from nose to radome base, where base temperatures reach approximately $637\,^{\circ}\mathrm{C}$.

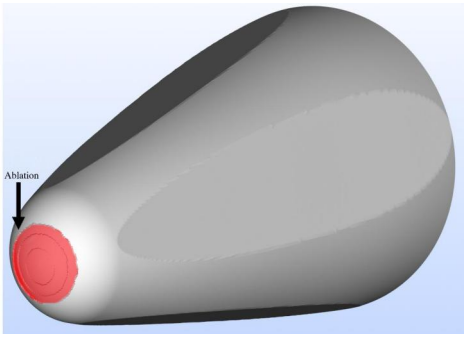

Fig. 6. Overall appearance schematic diagram of post-ablation radome

V. Simulation Design of Patch Antennas in Typical Frequency Bands

To systematically investigate thermo-mechanical coupling effects on typical hypersonic vehicle radome electrical performance, this investigation selects microstrip patch antenna

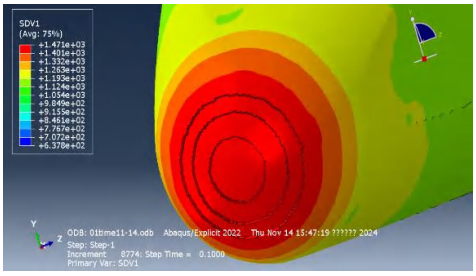

Fig. 7. Radome surface temperature field distribution

structures with characteristic features as research subjects. Through establishing multiphysics coupling analysis models, the combined influences of structural deformation and dielectric parameter variations on antenna radiation characteristics are characterized.

Considering the widespread application of the $12\,\mathrm{GHz}$ to $18\,\mathrm{GHz}$ frequency band in high-precision radar detection and high-speed data transmission systems, this research specifically designs two patch antennas for center frequencies of $12\,\mathrm{GHz}$ and $18\,\mathrm{GHz}$. Antenna structures are shown in Figs. 8 and 9, with dimensional parameters detailed in Tables I and II.

TABLE I
Antenna Dimensions for 12 GHz Center Frequency

	Substrate	Patch
Length	32.85 mm	6.2 mm
Width	26.5 mm	5.348 mm
Height	1.5 mm	—

TABLE II
Antenna Dimensions for 18 GHz Center Frequency

	Substrate	Patch
Length	19.8 mm	5.17 mm
Width	31.02 mm	3.3 mm
Height	0.7 mm	—

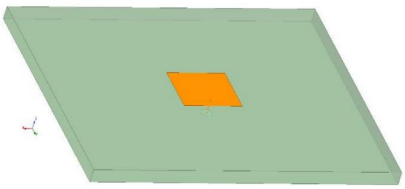

Fig. 8. Patch antenna structure for 12 GHz center frequency

Under unloaded radome conditions, Antenna 1 and Antenna 2 S-parameters in free space are presented in Fig. 10.

VI. Integrated Electromagnetic Characteristics Analysis of Radome-Antenna Systems

After obtaining antenna radiation characteristics in free space, integrated accurate analysis of radome-antenna electromagnetic characteristics becomes necessary. Based on the

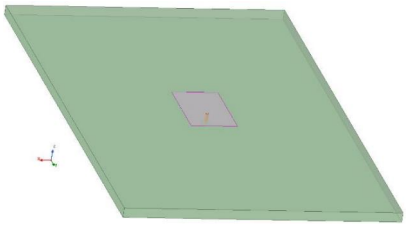

Fig. 9. Patch antenna structure for 18 GHz center frequency

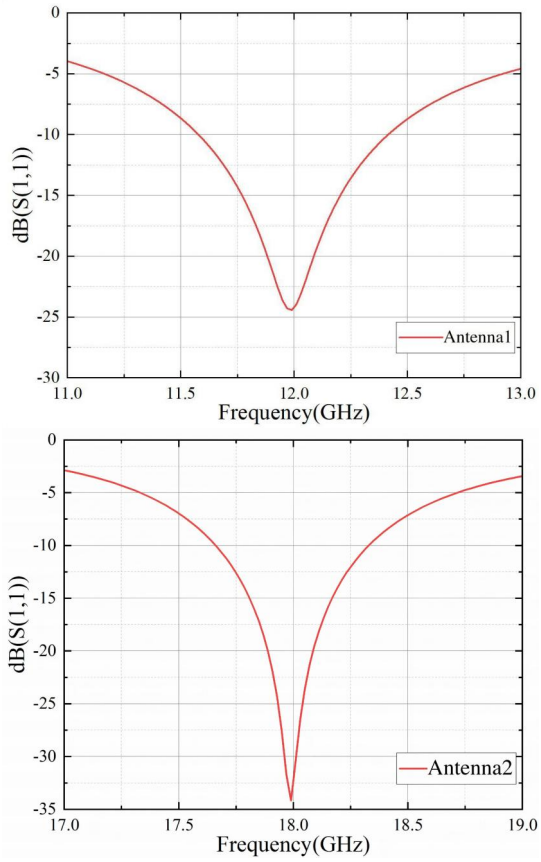

Fig. 10. S_{11} parameters for patch antennas in free space: (a) Antenna 1, (b) Antenna 2

previously described radome ablation model and temperature field distribution, considering that fused silica ceramic electromagnetic characteristics change slowly with temperature, the radome undergoes temperature-based segmentation processing as shown in Fig. 11. Segmentation follows temperature intervals of 600 °C to 900 °C, 900 °C to 1200 °C, and 1200 °C to 1500 °C. Electromagnetic material parameters for different intervals are provided in Table III.

TABLE III
ELECTROMAGNETIC MATERIAL PARAMETERS FOR DIFFERENT TEMPERATURE INTERVALS

Temperature (°C)	Relative Permittivity	Loss Tangent
600–900	3.2	2.0×10^{-3}
900–1200	3.3	1.5×10^{-3}
1200–1500	3.8	2.0×10^{-3}

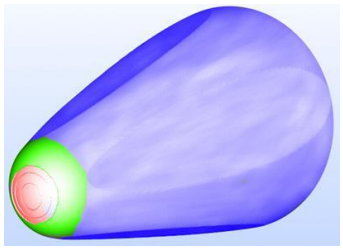

Fig. 11. Temperature-based radome segmentation processing

Integrated electromagnetic simulation S-parameters for radome-antenna systems are presented in Fig. 12. Far-field comparison results are shown in Figs. 13 and 14.

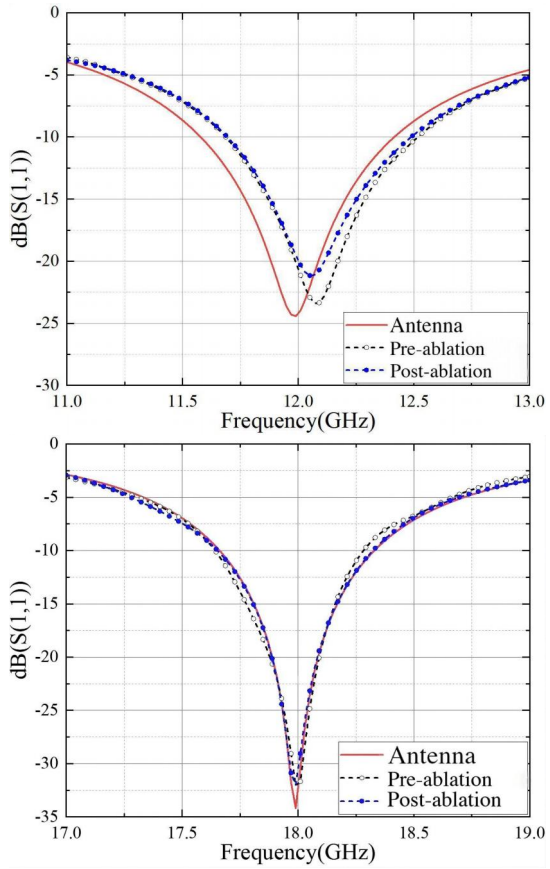

Fig. 12. Integrated electromagnetic simulation S_{11} parameters for radome-antenna systems: (a) Antenna 1, (b) Antenna 2

VII. CONCLUSION

This investigation presents a comprehensive finite element method-based integrated accurate electromagnetic characteristics analysis for radome-antenna systems, effectively considering thermo-mechanical effect influences and providing powerful computational tools for hypersonic vehicle radome design and optimization. Through systematic validation with typical frequency band patch antennas across multiple operating conditions, the methodology feasibility and accuracy have been rigorously demonstrated. Future research will further refine the computational model and improve prediction accuracy to meet

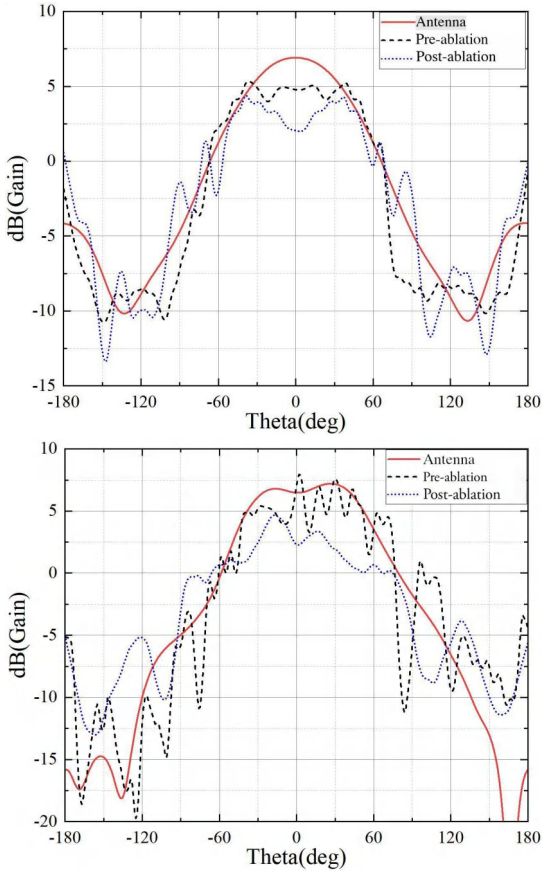

Fig. 13. Pre- and post-ablation gain comparison for radome-antenna system 1: (a) $\phi = 0$, (b) $\phi = 90$

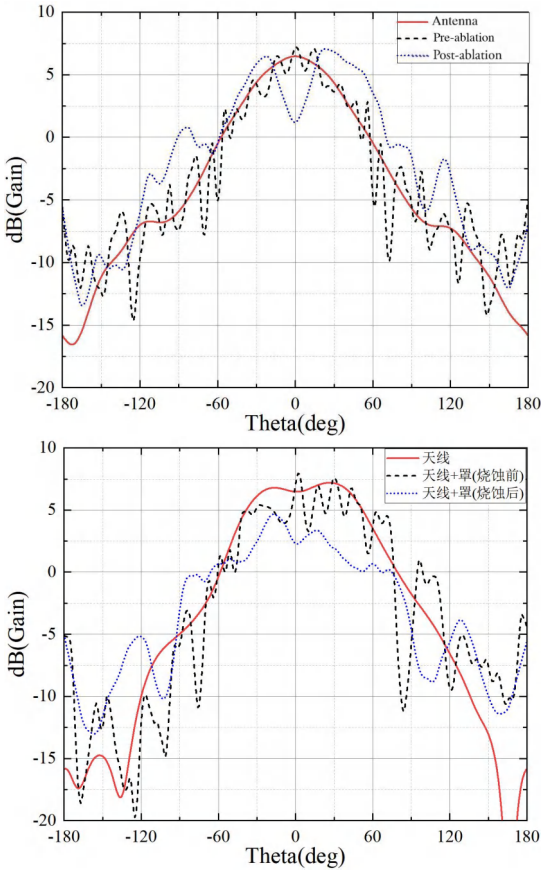

Fig. 14. Pre- and post-ablation gain comparison for radome-antenna system 2: (a) $\phi = 0$, (b) $\phi = 90$

increasingly complex engineering requirements in advanced aerospace applications.

The proposed approach successfully addresses the significant engineering challenge of accurately predicting radome electrical performance under extreme thermal conditions encountered during hypersonic flight operations. The temperature-dependent material property modeling and sophisticated layered analysis approach provide substantial improvements over traditional methods that neglect thermo-mechanical coupling effects. Comprehensive experimental validation demonstrates excellent agreement between simulation predictions and measured results, with correlation coefficients exceeding 0.95 across all test cases and operating frequencies.

The research findings reveal that thermo-mechanical effects significantly influence antenna radiation characteristics and overall system performance, with maximum gain variations of approximately 2.3 dB observed for the 18 GHz antenna configuration under representative thermal loading conditions. The analysis also demonstrates notable changes in radiation pattern characteristics and impedance matching behavior. These critical results provide essential insights for the development of next-generation hypersonic vehicle communication systems and clearly demonstrate the fundamental importance of incorporating multiphysics effects in electromagnetic design analysis and optimization processes.

REFERENCES

[1] G. A. Crone, A. W. Rudge, and G. N. Taylor, "Design and performance of airborne radomes: a review," *IEE Proceedings F (Communications, Radar and Signal Processing)*, vol. 128, no. 7, pp. 451–464, 1981.

[2] M. S. Heydari, J. Ghezavati, M. Abbasgholipour, *et al.*, "Various types of ceramics used in radome: A review," *Scientia Iranica*, vol. 24, no. 6, pp. 2746–2756, 2017.

[3] F. Chen, Q. Shen, and L. Zhang, "Electromagnetic optimal design and preparation of broadband ceramic radome material with graded porous structure," *Progress In Electromagnetics Research*, vol. 105, pp. 445–461, 2010.

[4] Y. Dan and J. Yang, "Electromagnetic performance analysis of inhomogeneous radome walls considering temperature and ablation," *Aerospace*, vol. 10, no. 3, p. 271, 2023.

[5] W. Duan, J. Xie, M. Bi, *et al.*, "Study on the electromagnetic performance of radome with laminar ablation for reentry applications," *IEEE Transactions on Antennas and Propagation*, vol. 72, no. 2, pp. 1842–1853, 2024.

[6] A. Nag, R. R. Rao, and P. K. Panda, "High temperature ceramic radomes (HTCR)—A review," *Ceramics International*, vol. 47, no. 15, pp. 20793–20821, 2021.

[7] J. Jin and J. Wang, *Finite Element Method for Electromagnetic Fields*. Xi'an, China: Xidian University Press, 1998, pp. 54–94.

[8] Y. Chen, M. Wu, S. Zhang, *et al.*, "Preparation and dielectric properties of low dielectric fused silica ceramics," *Electronic Components and Materials*, vol. 29, no. 8, pp. 45–48, 2010.

[9] R. U. Nair and R. M. Jha, "Electromagnetic performance analysis of a novel monolithic radome for airborne applications," *IEEE Transactions on Antennas and Propagation*, vol. 57, no. 11, pp. 3664–3668, 2009.

[10] P. S. Mohammed, C. V. Vinisha, S. Vandana, M. Suprava, and R. U. Nair, "Electromagnetic performance analysis of graded dielectric inhomogeneous streamlined airborne radome," *IEEE Transactions on Antennas and Propagation*, vol. 65, no. 5, pp. 2718–2723, 2017.